



Published in final edited form as:

J Magn Reson. 2022 August ; 341: 107256. doi:10.1016/j.jmr.2022.107256.

Nonparametric 5D $D-R_2$ distribution imaging with single-shot EPI at 21.1 T: Initial results for *in vivo* rat brain

Jens T. Rosenberg^a, Samuel C. Grant^{a,b}, Daniel Topgaard^{c,*}

^aNational High Magnetic Field Laboratory, Florida State University, Tallahassee FL, United States

^bChemical and Biomedical Engineering, FAMU-FSU College of Engineering, Florida State University, Tallahassee, FL, United States

^cPhysical Chemistry, Lund University, Lund, Sweden

Abstract

In vivo human diffusion MRI is by default performed using single-shot EPI with greater than 50-ms echo times and associated signal loss from transverse relaxation. The individual benefits of the current trends of increasing B_0 to boost SNR and employing more advanced signal preparation schemes to improve the specificity for selected microstructural properties eventually may be cancelled by increased relaxation rates at high B_0 and echo times with advanced encoding. Here, initial attempts to translate state-of-the-art diffusion-relaxation correlation methods from 3 T to 21.1 T are made to identify hurdles that need to be overcome to fulfill the promises of both high SNR and readily interpretable microstructural information.

Keywords

Multidimensional diffusion encoding; Diffusion-relaxation correlation; Ultra-high field; 21.1 T; Nonparametric 5D $D-R_2$; *In vivo*

1. Introduction

NMR diffusion-relaxation correlation methods [1–3] combined with data inversion into nonparametric distributions [4,5] of these MR properties have been applied successfully in low field studies of heterogeneity in materials ranging from porous rocks [6] to dairy products [7] and fruits [8] for decades. The methods more recently have been combined with MRI [9] and demonstrated to have great potential for both *ex vivo* [10–13] and *in vivo* [14] clinical applications as summarized in several comprehensive reviews during just the last

*Corresponding author at: Department of Chemistry, Lund University, P.O.B. 124, Lund, SE 221 00, Sweden.

daniel.topgaard@fkem1.lu.se (D. Topgaard).

Author statement

Jens T. Rosenberg: methodology, validation, investigation, resources, writing original draft and visualization. Samuel C. Grant: conceptualization, review and editing. Daniel Topgaard: conceptualization, methodology, software, validation, formal analysis, data curation, writing original draft, review and visualization.

Declaration of Competing Interest

The authors declare that they have no known competing financial interests or personal relationships that could have appeared to influence the work reported in this paper.

few years [14–17]. In addition, data challenges aimed to explore sub-sampling strategies has been performed aimed to harness the richness of information in multidimensional data with in feasible clinical scan times [18].

While most previous diffusion-relaxation studies have relied on the simple Stejskal-Tanner sequence [19] for which the effects of multiple aspects of molecular motion including bulk diffusivity, restriction, anisotropy, flow and exchange [20] are merged into apparent diffusion coefficients (ADCs) [21], a few studies [22–26] have incorporated more elaborate encoding strategies deriving from multidimensional solid-state NMR [27] to enable separation and correlation of parameters specific to the various types of motion. These multidimensional diffusion encoding methods build on carefully crafted gradient waveforms to attain selectivity at the expense of requiring higher gradients amplitudes or—when the maximum amplitudes are already reached—longer waveform durations than in conventional diffusion tensor imaging [28,29]. The resulting loss in signal-to-noise ratio (SNR) from transverse relaxation is in practice often compensated by using larger voxel sizes but could in principle be mitigated by ultra-high B_0 [30], the general benefits of which has been demonstrated for MRI and MR spectroscopy (MRS) in several papers [31–39].

So far, *in vivo* preclinical and human studies employing multidimensional or oscillating gradient diffusion encoding have been performed at 3 T [22–24,26,40–62], 4.7 T [63–65], 7 T [57,66–69], 9.4 T [70] and 11.7 T [71–73] while diffusion-relaxation correlation has been limited to 3 T [14,22–24,26]. All of these studies have relied on echo planar imaging (EPI) signal read-out, which allows for acquisition of a complete 2D image plane after a single excitation, but suffers from B_0 -dependent image distortions due to susceptibility inhomogeneity [31,74] and low SNR for materials with high transverse relaxation rate R_2 . As ultra-high B_0 systems are being developed also for *in vivo* human studies [30,75,76], we performed pilot measurements with multidimension diffusion-relaxation correlation and EPI readout at the highest field available for *in vivo* rodent, 21.1 T [77,78] to investigate the feasibility of translating pulse sequences from moderate to ultra-high B_0 and identify technical issues that need to be addressed to realize the full potential of combining diffusion-relaxation correlation, multidimensional diffusion encoding and ultra-high B_0 . Anticipating that transverse relaxation will be one of the main obstacles, we performed measurements yielding nonparametric joint distributions of R_2 and diffusion tensors \mathbf{D} [22,23].

2. Methods

2.1. MRI equipment

Experiments were performed using the 21.1-T magnet at the National High Magnetic Field Laboratory (NHMFL) in Tallahassee, FL [77,78]. The magnet was designed and built at the NHMFL, and is equipped with a Bruker Avance III console (Bruker-Biospin, MA, USA) using imaging gradients (Resonance Research Inc., MA, USA) capable of producing a gradient strength up to 600 mT/m. An in-house designed and built radio-frequency (RF) coil was used for all *in vitro* and *in vivo* experiments. The RF coil used was a double-saddle quadrature surface coil tuned to 900 MHz, the resonance frequency of ^1H at 21.1 T. The coil was built to accommodate the head of *in vivo* rodents weighing up to 350 g [34].

2.2. Phantoms

To validate the implementation of the multidimensional sequence on the 21.1-T magnet and for parameter optimization, a “Hex” liquid crystal phantom that provided high anisotropy was created as described by Nilsson *et al* [79]. In short, the phantom was placed in a 15-mL conical tube consisting of 41.94 wt% water (Milli-Q quality), 13.94 wt% of the hydrocarbon 2,2,4-trimethylpentane (Sigma-Aldrich, Sweden), and 44.12 wt% of the detergent sodium 1,4-bis(2-ethylhexoxy)-1,4-dioxobutane-2-sulfo nate (trade name AOT from Sigma-Aldrich, Sweden). At room temperature, the liquid crystal is in a reverse 2D hexagonal phase wherein water diffuses along cylindrical channels with ~ 5-nm diameters, which span lengths of hundreds of micrometers and gives rise to highly anisotropic diffusion. Around the 15-mL “Hex” phantom, two NMR tubes with 1-octanol (MilliporeSigma, MA, USA) and n-dodecane (TCI America, OR, USA) were placed. The combined tubes were secured and placed in a 50-mL conical tube filled with water. The phantom was secured into the RF coil and placed in the magnet.

2.3. Animals

Two Sprague Dawley rats weighing between 200 and 250 g were used. The animals were housed in cages with a 12-hour night/12-hour daylight cycle, with water and food available *ad libitum*. The animals were anesthetized with isoflurane (Baxter, IL, USA) and placed prone inside the coil with fore teeth placed on a bite bar. This bite bar also supplied a continuous flow of oxygen mixed with 1–3% of isoflurane. The concentration of isoflurane was set to maintain a steady respiration rate of 25–30 breaths per minute as monitored by a respiratory pillow (SA Instruments Inc., NY, USA) that was placed in between the rat and probe. Temperature was maintained at 37 °C by means of gradient chiller. The coil was tuned and matched for each individual rat for optimal performance. The same acquisition parameters used for the phantom were acquired for animals with the field-of-view (FOV) set to cover the head of the rat (32 × 11 mm). After confirming accurate placement of the rat, shimming was performed using either Bruker’s automatic B_0 shimming sequence or if needed adjusted by localized voxel placed over the parenchyma. All animal procedures were approved by the Florida State University (FSU) Animal Care and Use committee (ACUC).

2.4. MRI measurements

A ParaVision 6.0.1 implementation of a multi-slice 2D spin-echo EPI sequence with pairs of free gradient waveforms bracketing the 180° pulse [80] was kindly provided by Matthew Budde at the Medical College of Wisconsin (<https://osf.io/ngu4a>). The diffusion encoding tensor \mathbf{b} is obtained from the effective gradient $\mathbf{g}(t)$ via:

$$\mathbf{q}(t) = \gamma \int_0^t \mathbf{g}(t') dt', \quad (1)$$

and

$$\mathbf{b} = \int_0^{\text{TE}} \mathbf{q}(t) \mathbf{q}(t)^T dt, \quad (2)$$

where the integration is performed from the center of the excitation 90° pulse to the echo time τ_E . The sensitivity of the signal to anisotropy is controlled by the “shape” of \mathbf{b} , which is conveniently expressed by the normalized anisotropy b given by [81]:

$$b_\Delta = \frac{1}{b} \left(b_{ZZ} - \frac{b_{YY} + b_{XX}}{2} \right), \quad (3)$$

where b is the trace of \mathbf{b} and b_{XX} , b_{YY} , and b_{ZZ} are the eigenvalues ordered according to $(b_{ZZ} - b/3) > (b_{XX} - b/3) > (b_{YY} - b/3)$. Four 10-ms waveforms of the diffusion encoding gradients were used: linear ($b = 1$), planar ($b = -1/2$) and spherical ($b = 0$) as calculated in Ref. [82], as well as linear ($b = 1$) with a 5-ms half-sine pulse on each side of the 180° pulse. Gradient orientations (Θ , Φ) were obtained by the electrostatic repulsion scheme [83], and the number of directions were varied pseudo-randomly between 11 and 15 for the different values of τ_E within the range from 14.1 to 60 ms with an approximate logarithmic distribution. A detailed overview of the acquisition scheme can be found in in Fig. 1. Here gradient amplitude was varied between 10, 25, 45 and 80% (depending on diffusion scan) of peak gradient strength (0.6 T/m) The lowest and highest b-values were chosen to suppress spins undergoing flow, to achieve some attenuation of water spins with the lowest diffusivity, and were distributed logarithmically to improve sampling of the exponential signal decay [26,84]. Data was collected using nine slices of 1-mm thickness and FOV to cover the sample. Matrix was 140×48 (0.2×0.2 mm in-plane resolution) with a bandwidth of 500 kHz, two dummy scans and partial-FT encoding scheme (1.33 coverage). The repetition time (τ_R) was set to 5 s throughout, and the resultant total acquisition time was 120 min.

2.5. Data processing

After image reconstruction in ParaVision, data were exported to MatLab (R2018b MathWorks Inc, MA, USA) for denoising using random matrix theory [85]. In-plane motion and eddy correction with the MatLab routine *imregister* was used for in-plane affine registration, and Monte Carlo inversion [86] generated nonparametric 5D \mathbf{D} - R_2 distributions [22] using the *dtr2d* method in the *md-dmri* Matlab toolbox [87]. With this method, the signal $S(\mathbf{b}, \tau_E)$ acquired as a function of \mathbf{b} and τ_E at constant τ_R is approximated as originating from multiple sub-populations i , each being characterized by their weight w_i , diffusion tensor \mathbf{D}_i , and transverse relaxation rate $R_{2,i}$ according to:

$$S(\mathbf{b}, \tau_E) = \sum_i w_i \exp(-\tau_E R_{2,i}) \exp(-\mathbf{b} \cdot \mathbf{D}_i), \quad (4)$$

where the sum of w_i gives the non-encoded signal S_0 through:

$$S_0 = \sum_i w_i, \quad (5)$$

which is nominally proportional to the spin density.

Assuming diffusion with axial symmetry for each sub-population, the diffusion tensors are parameterized in terms of the axial and radial eigenvalues, $D_{A,i}$ and $D_{R,i}$ and orientation (θ_i, ϕ_i) . In this work, the Monte Carlo algorithm pseudo-randomly explores the parameter

space within the ranges $5 \cdot 10^{-12} \text{ m}^2\text{s}^{-1} < D_{A,i}, D_{R,i} < 5 \cdot 10^{-9} \text{ m}^2\text{s}^{-1}$ and $1 \text{ s}^{-1} < R_{2,i} < 80 \text{ s}^{-1}$ and—independently for each voxel—yields 100 solutions consistent with the input data. Each of these solutions comprises up to 20 components i characterized by the parameter set $[D_{A,i}, D_{R,i}, \theta_i, \phi_i, R_{2,i}]$ and the corresponding weights w_i . For visualization of the results, the values of $D_{A,i}$ and $D_{R,i}$ are converted to the isotropic diffusivity $D_{\text{iso},i}$ and squared normalized anisotropy $D_{\Delta,i}^2$ by [81,88]:

$$D_{\text{iso},i} = \frac{D_{A,i} + 2D_{R,i}}{3} \quad (6)$$

and

$$D_{\Delta,i}^2 = \left(\frac{D_{A,i} - D_{R,i}}{3D_{\text{iso},i}} \right)^2, \quad (7)$$

as well as the lab-frame diagonal elements $D_{xx,i}$, $D_{yy,i}$ and $D_{zz,i}$ according to standard equations. Single-voxel 5D \mathbf{D} - R_2 distributions are visualized by projecting the components onto the 2D $D_{\text{iso}} - D_{\Delta}^2$, $D_{\text{iso}} - R_2$, and $D_{\Delta}^2 - R_2$ planes, and parameter maps are generated by extracting means $E[x]$, variances $V[x]$, and covariances $C[x,y]$ according to [89]:

$$E[x] = \frac{\sum_i w_i x_i}{\sum_i w_i}, \quad (8)$$

$$V[x] = \frac{\sum_i w_i (x_i - E[x])^2}{\sum_i w_i}, \quad (9)$$

and

$$C[x, y] = \frac{\sum_i w_i (x_i - E[x])(y_i - E[y])}{\sum_i w_i}, \quad (10)$$

where x and y are various combinations of D_{iso} , D_{Δ}^2 , D_{xx} , D_{yy} , D_{zz} and R_2 . For comparison with results from conventional diffusion MRI performed at some finite value of τ_E , the relaxation factor can be included in the calculation of, for instance,

$$E^{(\tau_E)}[D_{\text{iso}}] = \frac{\sum_i w_i \exp(-\tau_E R_{2,i}) D_{\text{iso},i}}{\sum_i w_i \exp(-\tau_E R_{2,i})}, \quad (11)$$

which is closely related to the conventional a ADC [21] and mean diffusivity (MD) [28], and where “ τ_E ” serves as a reminder that the mean value includes weighting by R_2 relaxation during τ_E . An even more direct comparison with conventional ADC measured with a single b -value is obtained by:

$$\text{ADC}(b, \tau_E) = \frac{\ln S(b, \tau_E) - \ln S(0, \tau_E)}{b}, \quad (12)$$

where $\mathcal{S}(b, \tau_E)$ is given by Eq. (4).

The extraction of quantitative metrics according to Eqs. (8–10) are performed for each of the 100 individual solutions per voxel, and the values finally displayed in parameter maps are obtained by taking the medians of the results for the individual solutions.

3. Results

Fig. 2 shows signals and corresponding 5D $\mathbf{D}-R_2$ distributions for individual white matter (WM), gray matter (GM) and cerebral spinal fluid (CSF) voxels for a single representative rat brain. The S_0 maps are calculated according to Eq. (5), hence corresponding to signal at $TE = 0$ and $b = 0$. Consistent with previous *in vivo* mouse [90], *in vivo* human [22–24,26] and *ex vivo* rat results [25], the main distribution components of WM, GM and CSF are located in distinct corners of the 2D $D_{iso} - D_A^2$ projection (WM: low D_{iso} and high D_A^2 , GM: low D_{iso} and low D_A^2 , CSF: high D_{iso} and low D_A^2), thereby enabling “binning” for calculation of signal fractions f_{bin1} , f_{bin2} and f_{bin3} and associated diffusion-relaxation metrics nominally specific for WM, GM and CSF [22] as seen in Fig. 3a. The challenges of EPI readout at 21.1 T are readily apparent as distortions of the S_0 image stemming from susceptibility artifacts and Nyquist ghosting in the phase encoding direction [31,35]. Nevertheless, the bin-resolved fractions map captures the known spatial distributions of WM, GM and CSF. In addition to the binning, Fig. 3 also displays quantitative parameter maps obtained by extracting means $E[x]$, variances $V[x]$, and covariances $C[x,y]$ by applying Eqs. (8)–(10) over selected dimensions and sub-divisions of the per-voxel 5D $\mathbf{D}-R_2$ distributions [22–26,61,89,91]. The bin-resolved maps in Fig. 3b reveal $E[R_2]$ -values of 70 and 60 s^{-1} for WM and GM, respectively, which can be contrasted with the values 20 and 15 s^{-1} observed for *in vivo* human at 3 T [22]. The per-voxel $E[D_{iso}]$, $E[D_A^2]$ and $E[R_2]$ metrics in Fig. 3c are closely related to the more traditional parameters ADC [21] and MD [28], microscopic fractional anisotropy (μFA) [80,91], and quantitative $T_2 = 1/R_2$. Similar to μFA , the $E[D_A^2]$ metric provides information on diffusion anisotropy independently from the underlying degree of orientational order, which is in contrast to the traditional FA [80,91]. Intravoxel heterogeneity are described with the variance and covariance measures $V[x]$ and $C[x,y]$ for which x and y imply various combinations of D_{iso} , D_A^2 and R_2 . Out of all these measures, $V[D_{iso}]$ is most familiar from the literature under the names and symbols isotropic 2nd moment μ_2^{iso} [80], size variance V_{MD} [47] and isotropic mean kurtosis MK_1 [46], and has been shown to be related to intra-voxel variance of cell density in brain tumors [46]. A more detailed discussion about the biological meanings of the remaining heterogeneity metrics can be found in [25,26]. Low GW/WM contrast can be seen in certain structures, in particular the corpus callosum (cc), cerebellum and edges of white matter areas. This decrease is due to partial volume effects from the relatively large slice thickness but also from the chosen human brain-based boundary values for the various bins [90].

In Fig. 4, data from the phantom are presented. Here, the liquid crystal (red tube in Fig. 4a phantom cartoon), hydrocarbons (yellow and green tubes in Fig. 4a phantom cartoon) and water are used to emulate the diffusion properties of WM, GM and CSF, respectively

[79]. Even though the images are heavily distorted from chemical shift artifacts of the hydrocarbons and ghosting in the phase direction, the 21.1-T implementation of the 5D \mathbf{D} - R_2 method yield parameter maps consistent with the known diffusion and relaxation properties of the constituents of the phantom. Notably, the binning in the $D_{\text{iso}} - D_A^2$ plane designed for the calculation of tissue-specific signal fractions in the *in vivo* data also separates the liquid crystal, hydrocarbons and water fractions in the phantom data cleanly. For the liquid crystal, the directionally color-coded map $E[D_{xx}, D_{yy}, D_{zz}]$ clearly shows the structure of the anisotropic domains [82]. The magnetic susceptibility anisotropy results in an orientational dependence on T_2 and T_2^* as shown in Fig. 4c. These magnetic field dependent distortions are amplified at ultra-high fields as described by $B = \chi_m B_0$, where B is the field imposed by the tissue/material interface and perturbing B_0 by the magnetic susceptibility, χ_m , of the material [92]. Susceptibility differences in the phantom consequently exacerbate the warping artifact of the phantom that is not seen *in vivo*. Likewise, the low bandwidth in the phase encoding dimension together with the resonance frequency difference between the water and hydrocarbons leads to pronounced chemical shift displacements of the latter from the top to the lower part of the image.

4. Discussion

Reassuringly, the straightforward 21.1-T implementation of a standard EPI sequence broadly reproduces previous results from 3 T [22], however with noticeably lower signal on account of the nearly four-fold increase in R_2 and field gradients induced by differences in magnetic susceptibility.

The trend towards higher fields is expanding with 7 T becoming more applicable in the clinic [93–95] and now with extension to 11 T for animals as well as humans [30]. Discussions and a feasibility study for a 20-T human magnet further predicts future high field trends [75], showing the importance of translating these sequences to higher fields and identifying needs for improvements to overcome challenges introduced at these field strengths. Increased B_0 has many benefits such as SNR, spectral dispersion and higher spatial resolution, but also some impairments such as susceptibility and warping artifacts in EPI-based encoding due to susceptibility gradients and other artifacts that are amplified by low bandwidths [74]. Depending on the application, relaxation can benefit image contrast but also complicate quantitative assessment. Spin-lattice relaxation of tissues is generally increased with some convergence in values for different tissues, leading to a decreased contrast for T_1 -weighted scans. On the other hand, tissue signals are more readily saturated, benefiting contrast agent and time-of-flight applications. Transverse relaxation (T_2) times are generally shortened at increased field strength leading to improved blood oxygen saturation (BOLD) scans and susceptibility imaging, while also increasing the need for short TE scans to compensate for the decreased signal from shortened T_2 .

Published values of the ADC for the striatum of *in vivo* rat at 21.1 T cover the range from 0.7 to $0.8 \cdot 10^{-9} \text{ m}^2\text{s}^{-1}$ for image readout using simple spin echo, EPI, and spatio-temporal encoding (SPEN) at b -values up to $1 \cdot 10^9 \text{ sm}^{-2}$ and values of τ_E in the range from 25 to 40 ms [31]. For comparison with literature data, ADC values were calculated from $S(b, \tau_E)$

images synthesized from the 5D \mathbf{D} - R_2 distributions according to Eq. (12), yielding $\text{ADC} = (0.78 \pm 0.04) 10^{-9} \text{ m}^2\text{s}^{-1}$ (mean \pm standard deviation) at $b = 1 \cdot 10^9 \text{ sm}^{-2}$ and $\tau_E = 30 \text{ ms}$, which can be contrasted with $E[D_{\text{iso}}] = (0.99 \pm 0.09) 10^{-9} \text{ m}^2\text{s}^{-1}$ corresponding to ADC in the limit $b = 0$ and $\tau_E = 0$.

To capitalize on the potential SNR gains by ultra-high field, advanced diffusion sequences may require correspondingly ultra-strong gradients [38,39,60,96–98] to minimize the duration of typically lengthy gradient waveforms and, image read-out approaches. SPEN [31,35,90,99] or gradient and spin echo (GRASE) [100] are examples of such approaches that are less susceptible to B_0 inhomogeneity and relaxation than single-shot EPI. SPEN has been used at 21.1-T and has shown that B_0 artifacts can be overcome despite the minimum τ_E being longer than that of traditional spin-echo EPI [31,35]. With SPEN, τ_E increases linearly with the spatial coordinate in the low-bandwidth dimension, producing a gradient in T_2 -weighting that potentially can produce a bias in diffusion metrics. Yon *et al.* has expanded on SPEN readout and incorporated the multidimensional diffusion approach at 15.2 T [79, 90]. In doing so, Yon *et al.* employed SPEN in its fully refocusing mode and increased bandwidth to reduce B_0 inhomogeneity artifacts without compromising diffusion tensor distribution metrics from the incorporated multidimensional diffusion acquisition scheme [90]. In addition, Yon *et al.* [101] showed that the SPEN technique alleviated artifacts in distortion prone regions of mouse brains for diffusion tensor imaging (DTI). Interleaved multi-segmented EPI acquisitions at 21.1 T also have been shown to reduce echo times and alleviate geometric distortions; however, this approach did not provide reliable ADC values, potentially due to motion or sampling impacts on signal [31]. Notably, the current study, as with other single-shot EPI readouts acquisitions [31,35], did provide expected and reliable diffusion measures. Persistent geometric distortions and artifacts are particularly prevalent in the composite phantom for which susceptibility mismatches together with chemical shift significantly reduce image quality. Nevertheless, as shown not only in this report but also others, *in vivo* and phantom diffusion data are accurate quantitatively [31,35,79]. There are other strategies that can be implemented for future work that are commonly used in clinical settings to correct for EPI or field inhomogeneities, such as acquiring B_0 maps or inverted EPI blips. Other corrections such as brain/skull extraction, signal drift correction, denoising, etc [102] to improve data visualization should be considered for future work but may not be relevant in a preclinical setting.

5. Conclusion

In this study, it has been shown that an advanced diffusion scheme such as the multidimensional diffusion can be implemented at 21.1 T to provide results consistent with previous lower field studies. To realize the full potential of ultra-high field, efforts need to be directed to both sequence design and gradient hardware improvements to minimize warping artifacts and reach even shorter values of τ_E .

Acknowledgement

The authors appreciate the assistance of the staff and scientists of the US National High Magnetic Field Laboratory, as well as the gradient waveforms made available by Matthew Budde at the Medical College of Wisconsin. This work was financially supported the Swedish Foundation for Strategic Research, (ITM17-0267) and Swedish

Research Council (2018-03697) to DT and the US National Institutes of Health (R01-NS102395) to SCG. DT owns shares in Random Walk Imaging AB (Lund, Sweden, <http://www.rwi.se/>), holding patents related to the described methods. The US National High Magnetic Field Laboratory is supported by the US National Science Foundation (DMR-1644779) and the State of Florida.

References

- [1]. Galvosas P, Callaghan PT, Multi-dimensional inverse Laplace spectroscopy in the NMR of porous media, *Compt. Rendus Phys* 11 (2010) 172–180, 10.1016/j.crhy.2010.06.014.
- [2]. Bernin D, Topgaard D, NMR diffusion and relaxation correlation methods: New insights in heterogeneous materials, *Curr. Opin. Colloid Interface Sci* 18 (2013) 166–172, 10.1016/j.cocis.2013.03.007.
- [3]. Song Y-Q, Venkataramanan L, Kausik R, Heaton N, Chapter 4:Two-dimensional NMR of Diffusion and Relaxation, *Diffus. NMR Confin. Syst*, 2016, p. 111–55. 10.1039/9781782623779-00111.
- [4]. Benjamini D, Chapter 10:Nonparametric Inversion of Relaxation and Diffusion Correlation Data. *Adv. Diffus. Encoding Methods MRI*, 2020, p. 278–316. 10.1039/9781788019910-00278.
- [5]. Mitchell J, Chandrasekera TC, Gladden LF, Numerical estimation of relaxation and diffusion distributions in two dimensions, *Prog. Nucl. Magn. Reson. Spectrosc* 62 (2012) 34–50, 10.1016/j.pnmrs.2011.07.002. [PubMed: 22364615]
- [6]. Xie R, Xiao L, Advanced fluid-typing methods for NMR logging, *Pet. Sci* 8 (2011) 163–169, 10.1007/s12182-011-0130-4.
- [7]. Hürlimann MD, Burcaw L, Song Y-Q, Quantitative characterization of food products by two-dimensional D-T2 and T1–T2 distribution functions in a static gradient, *J. Colloid Interface Sci* 297 (2006) 303–311, 10.1016/j.jcis.2005.10.047. [PubMed: 16300777]
- [8]. Marigheto N, Venturi L, Hills B, Two-dimensional NMR relaxation studies of apple quality, *Postharvest Biol. Technol* 48 (2008) 331–340, 10.1016/j.postharvbio.2007.11.002.
- [9]. Zhang Y, Blümich B, Spatially resolved D-T2 correlation NMR of porous media, *J. Magn. Reson* 242 (2014) 41–48, 10.1016/j.jmr.2014.01.017. [PubMed: 24607821]
- [10]. Kim D, Doyle EK, Wisnowski JL, Kim JH, Haldar JP, Diffusion-relaxation correlation spectroscopic imaging: A multidimensional approach for probing microstructure, *Magn. Reson. Med* 78 (2017) 2236–2249, 10.1002/mrm.26629. [PubMed: 28317261]
- [11]. Benjamini D, Basser PJ, Magnetic resonance microdynamic imaging reveals distinct tissue microenvironments, *NeuroImage* 163 (2017) 183–196, 10.1016/j.neuroimage.2017.09.033. [PubMed: 28943412]
- [12]. Benjamini D, Iacono D, Komlosh ME, Perl DP, Brody DL, Basser PJ, Diffuse axonal injury has a characteristic multidimensional MRI signature in the human brain, *Brain J. Neurol* 144 (2021) 800–816, 10.1093/brain/awaa447.
- [13]. Zhang Z, Wu HH, Priester A, Magyar C, Afshari Mirak S, Shakeri S, et al. , Prostate Microstructure in Prostate Cancer Using 3-T MRI with Diffusion-Relaxation Correlation Spectrum Imaging: Validation with Whole-Mount Digital Histopathology, *Radiology* 296 (2020) 348–355, 10.1148/radiol.2020192330. [PubMed: 32515678]
- [14]. Slator PJ, Hutter J, Palombo M, Jackson LH, Ho A, Panagiotaki E, et al. , Combined diffusion-relaxometry MRI to identify dysfunction in the human placenta, *Magn. Reson. Med* 82 (2019) 95–106, 10.1002/mrm.27733. [PubMed: 30883915]
- [15]. Tax CMW, Estimating chemical and microstructural heterogeneity by correlating relaxation and diffusion, in: Topgaard D, editor. *Adv. Diffus. Encoding Methods MRI*, Cambridge (UK): Royal Society of Chemistry; 2020.
- [16]. Kim D, Wisnowski JL, Nguyen CT, Haldar JP, Multidimensional correlation spectroscopic imaging of exponential decays: From theoretical principles to in vivo human applications, *NMR Biomed.* 33 (2020), 10.1002/nbm.4244 e4244. [PubMed: 31909534]
- [17]. Benjamini D, Basser PJ, Multidimensional correlation MRI, *NMR Biomed.* 33 (2020), 10.1002/nbm.4226 e4226. [PubMed: 31909516]

- [18]. Pizzolato M, Palombo M, Bonet-Carne E, Tax CMW, Grussu F, Ianus A, et al. Acquiring and Predicting Multidimensional Diffusion (MUDI) Data: An Open Challenge. In: Bonet-Carne E, Hutter J, Palombo M, Pizzolato M, Sepehrband F, Zhang F, editors. *Comput. Diffus. MRI*, Cham: Springer International Publishing; 2020, p. 195–208.
- [19]. Stejskal EO, Tanner JE, Spin echoes in the presence of a time dependent gradient field, *J. Chem. Phys* 42 (1965).
- [20]. Topgaard D, Multiple dimensions for random walks, *J. Magn. Reson* 306 (2019) 150–154, 10.1016/j.jmr.2019.07.024. [PubMed: 31307891]
- [21]. Le Bihan D, Breton E, Lallemand D, Grenier P, Cabanis E, Laval-Jeantet M, MR imaging of intravoxel incoherent motions: application to diffusion and perfusion in neurologic disorders, *Radiology* 161 (1986) 401–407, 10.1148/radiology.161.2.3763909. [PubMed: 3763909]
- [22]. de Almeida Martins JP, Tax CMW, Szczepankiewicz F, Jones DK, Westin C-F, Topgaard D, Transferring principles of solid-state and Laplace NMR to the field of in vivo brain MRI, *Magn. Reson* 1 (2020) 27–43, 10.5194/mr-1-27-2020.
- [23]. Martins JP de A, Tax CMW, Reymbaut A, Szczepankiewicz F, Chamberland M, Jones DK, et al. Computing and visualising intra-voxel orientation-specific relaxation–diffusion features in the human brain. *Hum Brain Mapp* 2021;42:310–28. 10.1002/hbm.25224. [PubMed: 33022844]
- [24]. Reymbaut A, Critchley J, Durighel G, Sprenger T, Sughrue M, Bryskhe K, et al. , Toward nonparametric diffusion-T1 characterization of crossing fibers in the human brain, *Magn. Reson. Med* 85 (2021) 2815–2827, 10.1002/mrm.28604. [PubMed: 33301195]
- [25]. Narvaez O, Svenningsson L, Yon M, Sierra A, Topgaard D, Massively Multidimensional Diffusion-Relaxation Correlation MRI, *Front. Phys* 9 (2022).
- [26]. Martin J, Reymbaut A, Schmidt M, Doerfler A, Uder M, Laun FB, et al. , Nonparametric D-R1-R2 distribution MRI of the living human brain, *NeuroImage* 245 (2021), 10.1016/j.neuroimage.2021.118753118753.
- [27]. Topgaard D, Multidimensional diffusion MRI, *J. Magn. Reson* 275 (2017) 98–113, 10.1016/j.jmr.2016.12.007. [PubMed: 28040623]
- [28]. Basser PJ, Mattiello J, LeBihan D, MR diffusion tensor spectroscopy and imaging, *Biophys. J* 66 (1994) 259–267, 10.1016/S0006-3495(94)80775-1. [PubMed: 8130344]
- [29]. Pierpaoli C, Jezzard P, Basser PJ, Barnett A, Di Chiro G, Diffusion tensor MR imaging of the human brain, *Radiology* 201 (1996) 637–648, 10.1148/radiology.201.3.8939209. [PubMed: 8939209]
- [30]. Bihan DL, Schild T, Human brain MRI at 500 MHz, scientific perspectives and technological challenges, *Supercond. Sci. Technol* 30 (2017), 10.1088/1361-6668/30/3/033003 033003.
- [31]. Leftin A, Rosenberg JT, Solomon E, Bejarano FC, Grant SC, Frydman L. Ultrafast in vivo diffusion imaging of stroke at 21.1 T by spatiotemporal encoding. *Magn Reson Med Off J Soc Magn Reson Med Soc Magn Reson Med* 2015;73:1483. 10.1002/mrm.25271.
- [32]. Shemesh N, Rosenberg JT, Dumez JN, Grant SC, Frydman L, Metabolic T1 dynamics and longitudinal relaxation enhancement in vivo at ultrahigh magnetic fields on ischemia, *J Cereb Blood Flow Metab Off J Int Soc Cereb Blood Flow Metab* 34 (2014) 1810–1817, 10.1038/jcbfm.2014.149 [doi].
- [33]. Shemesh N, Rosenberg JT, Dumes J-N, Muniz JA, Grant SC, Frydman L, Metabolic properties in stroked rats revealed by relaxation-enhanced magnetic resonance spectroscopy at ultrahigh fields, *NatComm* 5 (2014) 4958, 10.1038/ncomms5958.
- [34]. Rosenberg JT, Shemesh N, Muniz JA, Dumez JN, Frydman L, Grant SC, Transverse relaxation of selectively excited metabolites in stroke at 21.1 T, *Magn. Reson. Med* (2016), 10.1002/mrm.26132 [doi].
- [35]. Leftin A, Rosenberg JT, Yuan X, Ma T, Grant SC, Frydman L. Multiparametric classification of sub-acute ischemic stroke recovery with ultrafast diffusion, ²³Na, and MPIO-labeled stem cell MRI at 21.1 T. *NMR Biomed* 2020;33: e4186. 10.1002/nbm.4186. [PubMed: 31797472]
- [36]. Abad N, Rosenberg JT, Roussel T, Grice DC, Harrington MG, Grant SC, Metabolic assessment of a migraine model using relaxation-enhanced (1) H spectroscopy at ultrahigh field, *Magn. Reson. Med* 79 (2018) 1266–1275, 10.1002/mrm.26811 [doi]. [PubMed: 28921630]

- [37]. Bagdasarian FA, Yuan X, Athey J, Bunnell BA, Grant SC, NODDI highlights recovery mechanisms in white and gray matter in ischemic stroke following human stem cell treatment, *Magn. Reson. Med* 86 (2021) 3211, 10.1002/mrm.28929. [PubMed: 34355818]
- [38]. Jespersen SN, Olesen JL, Ianus A, Shemesh N, Effects of nongaussian diffusion on “isotropic diffusion” measurements: An ex-vivo microimaging and simulation study, *J. Magn. Reson* 300 (2019) 84–94, 10.1016/j.jmr.2019.01.007. [PubMed: 30711786]
- [39]. Ianus A, Jespersen SN, Serradas Duarte T, Alexander DC, Drobnjak I, Shemesh N, Accurate estimation of microscopic diffusion anisotropy and its time dependence in the mouse brain, *NeuroImage* 183 (2018) 934–949, 10.1016/j.neuroimage.2018.08.034. [PubMed: 30145206]
- [40]. Nilsson M, Lätt J, van Westen D, Brockstedt S, Lasi S, Ståhlberg F, et al. , Noninvasive mapping of water diffusional exchange in the human brain using filter-exchange imaging, *Magn. Reson. Med* 69 (2013) 1572–1580, 10.1002/mrm.24395.
- [41]. Lampinen B, Szczepankiewicz F, van Westen D, Englund E, Sundgren PC, Lätt J, et al. , Optimal experimental design for filter exchange imaging: Apparent exchange rate measurements in the healthy brain and in intracranial tumors, *Magn. Reson. Med* 77 (2017) 1104–1114, 10.1002/mrm.26195. [PubMed: 26968557]
- [42]. Avram AV, Özarslan E, Sarlls JE, Basser PJ, In vivo detection of microscopic anisotropy using quadruple pulsed-field gradient (qPFG) diffusion MRI on a clinical scanner, *NeuroImage* 64 (2013) 229–239, 10.1016/j.neuroimage.2012.08.048. [PubMed: 22939872]
- [43]. Lawrenz M, Finsterbusch J, Double-wave-vector diffusion-weighted imaging reveals microscopic diffusion anisotropy in the living human brain, *Magn. Reson. Med* 69 (2013) 1072–1082, 10.1002/mrm.24347. [PubMed: 22711603]
- [44]. Szczepankiewicz F, Lasi S, van Westen D, Sundgren PC, Englund E, Westin C-F, et al. , Quantification of microscopic diffusion anisotropy disentangles effects of orientation dispersion from microstructure: Applications in healthy volunteers and in brain tumors, *NeuroImage* 104 (2015) 241–252, 10.1016/j.neuroimage.2014.09.057. [PubMed: 25284306]
- [45]. Lawrenz M, Finsterbusch J, Mapping measures of microscopic diffusion anisotropy in human brain white matter in vivo with double-wave-vector diffusion-weighted imaging, *Magn. Reson. Med* 73 (2015) 773–783, 10.1002/mrm.25140. [PubMed: 24469974]
- [46]. Szczepankiewicz F, van Westen D, Englund E, Westin C-F, Ståhlberg F, Lätt J, et al. , The link between diffusion MRI and tumor heterogeneity: Mapping cell eccentricity and density by diffusional variance decomposition (DIVIDE), *NeuroImage* 142 (2016) 522–532, 10.1016/j.neuroimage.2016.07.038. [PubMed: 27450666]
- [47]. Westin C-F, Knutsson H, Pasternak O, Szczepankiewicz F, Özarslan E, van Westen D, et al. , Q-space trajectory imaging for multidimensional diffusion MRI of the human brain, *NeuroImage* 135 (2016) 345–362, 10.1016/j.neuroimage.2016.02.039. [PubMed: 26923372]
- [48]. L M, B S, F J. Microscopic diffusion anisotropy in the human brain: Age-related changes. *Neuroimage* 2016;141:313–25. 10.1016/j.neuroimage.2016.07.031. [PubMed: 27436594]
- [49]. Lampinen B, Szczepankiewicz F, Mårtensson J, van Westen D, Sundgren PC, Nilsson M, Neurite density imaging versus imaging of microscopic anisotropy in diffusion MRI: A model comparison using spherical tensor encoding, *NeuroImage* 147 (2017) 517–531, 10.1016/j.neuroimage.2016.11.053. [PubMed: 27903438]
- [50]. Yang G, Tian Q, Leuze C, Wintermark M, McNab JA, Double diffusion encoding MRI for the clinic, *Magn. Reson. Med* 80 (2018) 507–520, 10.1002/mrm.27043. [PubMed: 29266375]
- [51]. Avram AV, Sarlls JE, Basser PJ, Measuring non-parametric distributions of intravoxel mean diffusivities using a clinical MRI scanner, *NeuroImage* 185 (2019) 255–262, 10.1016/j.neuroimage.2018.10.030. [PubMed: 30326294]
- [52]. Lampinen B, Szczepankiewicz F, Novén M, van Westen D, Hansson O, Englund E, et al. , Searching for the neurite density with diffusion MRI: Challenges for biophysical modeling, *Hum. Brain Mapp* 40 (2019) 2529–2545, 10.1002/hbm.24542. [PubMed: 30802367]
- [53]. Lawrenz M, Finsterbusch J, Detection of microscopic diffusion anisotropy in human cortical gray matter in vivo with double diffusion encoding, *Magn. Reson. Med* 81 (2019) 1296–1306, 10.1002/mrm.27451. [PubMed: 30206991]

- [54]. Nery F, Szczepankiewicz F, Kerkelä L, Hall MG, Kaden E, Gordon I, et al. , In vivo demonstration of microscopic anisotropy in the human kidney using multidimensional diffusion MRI, *Magn. Reson. Med* 82 (2019) 2160–2168, 10.1002/mrm.27869. [PubMed: 31243814]
- [55]. Yang G, McNab JA, Eddy current nulled constrained optimization of isotropic diffusion encoding gradient waveforms, *Magn. Reson. Med* 81 (2019) 1818–1832, 10.1002/mrm.27539. [PubMed: 30368913]
- [56]. Lampinen B, Szczepankiewicz F, Mårtensson J, van Westen D, Hansson O, Westin C-F, et al. , Towards unconstrained compartment modeling in white matter using diffusion-relaxation MRI with tensor-valued diffusion encoding, *Magn. Reson. Med* 84 (2020) 1605–1623, 10.1002/mrm.28216. [PubMed: 32141131]
- [57]. Lampinen B, Zampeli A, Björkman-Burtscher IM, Szczepankiewicz F, Källén K, Strandberg MC, et al. , Tensor-valued diffusion MRI differentiates cortex and white matter in malformations of cortical development associated with epilepsy, *Epilepsia* 61 (2020) 1701–1713, 10.1111/epi.16605. [PubMed: 32667688]
- [58]. Nilsson M, Szczepankiewicz F, Brabec J, Taylor M, Westin C, Golby A, et al. , Tensor-valued diffusion MRI in under 3 minutes: an initial survey of microscopic anisotropy and tissue heterogeneity in intracranial tumors, *Magn. Reson. Med* 83 (2020) 608–620, 10.1002/mrm.27959. [PubMed: 31517401]
- [59]. Andersen KW, Lasi S, Lundell H, Nilsson M, Topgaard D, Sellebjerg F, et al. Disentangling white-matter damage from physiological fibre orientation dispersion in multiple sclerosis. *Brain Commun* 2020;2:fcaa077. 10.1093/braincomms/fcaa077. [PubMed: 32954329]
- [60]. Tan ET, Shih RY, Mitra J, Sprenger T, Hua Y, Bhushan C, et al. , Oscillating diffusion-encoding with a high gradient-amplitude and high slew-rate head-only gradient for human brain imaging, *Magn. Reson. Med* 84 (2020) 950–965, 10.1002/mrm.28180. [PubMed: 32011027]
- [61]. Naranjo ID, Reymbaut A, Brynolfsson P, Lo Gullo R, Bryskhe K, Topgaard D, et al. , Multidimensional Diffusion Magnetic Resonance Imaging for Characterization of Tissue Microstructure in Breast Cancer Patients: A Prospective Pilot Study, *Cancers* 13 (2021) 1606, 10.3390/cancers13071606. [PubMed: 33807205]
- [62]. Novello L, Henriques RN, Ianus A, Feiweier T, Shemesh N, Jovicich J, In vivo Correlation Tensor MRI reveals microscopic kurtosis in the human brain on a clinical 3T scanner, *NeuroImage* 254 (2022), 10.1016/j.neuroimage.2022.119137 119137. [PubMed: 35339682]
- [63]. Baron CA, Beaulieu C, Oscillating gradient spin-echo (OGSE) diffusion tensor imaging of the human brain, *Magn. Reson. Med* 72 (2014) 726–736, 10.1002/mrm.24987. [PubMed: 24142863]
- [64]. Baron CA, Kate M, Gioia L, Butcher K, Emery D, Budde M, et al. , Reduction of Diffusion-Weighted Imaging Contrast of Acute Ischemic Stroke at Short Diffusion Times, *Stroke* 46 (2015) 2136–2141, 10.1161/STROKEAHA.115.008815. [PubMed: 26152297]
- [65]. Does MD, Parsons EC, Gore JC, Oscillating gradient measurements of water diffusion in normal and globally ischemic rat brain, *Magn. Reson. Med* 49 (2003) 206–215, 10.1002/mrm.10385. [PubMed: 12541239]
- [66]. Maximov II, Vellmer S, Isotropically weighted intravoxel incoherent motion brain imaging at 7T, *Magn. Reson. Imag* 57 (2019) 124–132, 10.1016/j.mri.2018.11.007.
- [67]. Szczepankiewicz F, Sjölund J, Ståhlberg F, Lätt J, Nilsson M, Tensor-valued diffusion encoding for diffusional variance decomposition (DIVIDE): Technical feasibility in clinical MRI systems, *PLoS ONE* 14 (2019), 10.1371/journal.pone.0214238 e0214238. [PubMed: 30921381]
- [68]. Arbabi A, Kai J, Khan AR, Baron CA, Diffusion dispersion imaging: Mapping oscillating gradient spin-echo frequency dependence in the human brain, *Magn. Reson. Med* 83 (2020) 2197–2208, 10.1002/mrm.28083. [PubMed: 31762110]
- [69]. Shemesh N, Barazany D, Sadan O, Bar L, Zur Y, Barhum Y, et al. , Mapping apparent eccentricity and residual ensemble anisotropy in the gray matter using angular double-pulsed-field-gradient MRI, *Magn. Reson. Med* 68 (2012) 794–806, 10.1002/mrm.23300. [PubMed: 22128033]
- [70]. Alves R, Henriques RN, Kerkelä L, Chavarrías C, Jespersen SN, Shemesh N, Correlation Tensor MRI deciphers underlying kurtosis sources in stroke, *NeuroImage* 247 (2022), 10.1016/j.neuroimage.2021.118833 118833. [PubMed: 34929382]

- [71]. Wu D, Martin LJ, Northington FJ, Zhang J, Oscillating gradient diffusion MRI reveals unique microstructural information in normal and hypoxiaischemia injured mouse brains, *Magn. Reson. Med* 72 (2014) 1366–1374, 10.1002/mrm.25441. [PubMed: 25168861]
- [72]. Aggarwal M, Jones MV, Calabresi PA, Mori S, Zhang J, Probing mouse brain microstructure using oscillating gradient diffusion MRI, *Magn Reson Med* 67 (2012) 98–109, 10.1002/mrm.22981. [PubMed: 21590726]
- [73]. Wu D, Zhang J, The Effect of Microcirculatory Flow on Oscillating Gradient Diffusion MRI and Diffusion Encoding with Dual-Frequency Orthogonal Gradients (DEFOG), *Magn Reson Med* 77 (2017) 1583–1592, 10.1002/mrm.26242. [PubMed: 27080566]
- [74]. Jezzard P, Balaban RS, Correction for geometric distortion in echo planar images from B0 field variations, *Magn Reson Med* 34 (1995) 65–73, 10.1002/mrm.1910340111. [PubMed: 7674900]
- [75]. Budinger TF, Bird MD, Frydman L, Long JR, Mareci TH, Rooney WD, et al. , Toward 20 T magnetic resonance for human brain studies: opportunities for discovery and neuroscience rationale, *Magma* 29 (2016) 617–639, 10.1007/s10334-016-0561-4. [PubMed: 27194154]
- [76]. Budinger TF, Bird MD, MRI and MRS of the human brain at magnetic fields of 14T to 20T: Technical feasibility, safety, and neuroscience horizons, *NeuroImage* 168 (2018) 509–531, 10.1016/j.neuroimage.2017.01.067. [PubMed: 28179167]
- [77]. Fu R, Brey WW, Shetty K, Gor'kov P, Saha S, Long JR, et al. Ultra-wide bore 900 MHz high-resolution NMR at the National High Magnetic Field Laboratory. *J Magn Reson San Diego Calif* 1997 2005;177:1–8. 10.1016/j.jmr.2005.07.013.
- [78]. Markiewicz WD, Brey WW, Cross TA, Dixon IR, Gor'kov PL, Grant SC, et al. A Decade of Experience With the UltraWide-Bore 900-MHz NMR Magnet. *IEEE Trans Appl Supercond* 2015;25.
- [79]. Nilsson M, Larsson J, Lundberg D, Szczepankiewicz F, Witzel T, Westin C-F, et al. , Liquid crystal phantom for validation of microscopic diffusion anisotropy measurements on clinical MRI systems, *Magn Reson Med* 79 (2018) 1817–1828, 10.1002/mrm.26814. [PubMed: 28686785]
- [80]. Lasi S, Szczepankiewicz F, Eriksson S, Nilsson M, Topgaard D, Microanisotropy imaging: quantification of microscopic diffusion anisotropy and orientational order parameter by diffusion MRI with magic-angle spinning of the q-vector, *Front Phys* 2 (2014), 10.3389/fphy.2014.00011.
- [81]. Eriksson S, Lasi S, Nilsson M, Westin C-F, Topgaard D, NMR diffusion-encoding with axial symmetry and variable anisotropy: Distinguishing between prolate and oblate microscopic diffusion tensors with unknown orientation distribution, *J Chem Phys* 142 (2015), 10.1063/1.4913502 104201. [PubMed: 25770532]
- [82]. Topgaard D, Director orientations in lyotropic liquid crystals: diffusion MRI mapping of the Saupe order tensor, *Phys Chem Chem Phys* PCCP 18 (2016) 8545–8553, 10.1039/c5cp07251d. [PubMed: 26948308]
- [83]. null Bak, null Nielsen. REPULSION, A Novel Approach to Efficient Powder Averaging in Solid-State NMR. *J Magn Reson San Diego Calif* 1997 1997;125:132–9. 10.1006/jmre.1996.1087.
- [84]. Istratov AA, Vyvenko OF, Exponential analysis in physical phenomena, *Rev Sci Instrum* 70 (1999) 1233–1257, 10.1063/1.1149581.
- [85]. Veraart J, Fieremans E, Novikov DS, Diffusion MRI noise mapping using random matrix theory, *Magn Reson Med* 76 (2016) 1582–1593, 10.1002/mrm.26059. [PubMed: 26599599]
- [86]. M P, Yq S. Quantifying uncertainty in NMR T2 spectra using Monte Carlo inversion. *J Magn Reson San Diego Calif* 1997 2008;196:54–60. 10.1016/j.jmr.2008.10.008.
- [87]. Nilsson M, Szczepankiewicz F, Lampinen B, Ahlgren A, de Almeida Martins JP, Lasi S, et al. , An open-source framework for analysis of multidimensional diffusion MRI data implemented in MATLAB, *Proceeding Int. Soc. Magn. Reson. Med, Paris, France, 2018.*
- [88]. Conturo TE, McKinstry RC, Akbudak E, Robinson BH, Encoding of anisotropic diffusion with tetrahedral gradients: a general mathematical diffusion formalism and experimental results, *Magn Reson Med* 35 (1996) 399–412, 10.1002/mrm.1910350319. [PubMed: 8699953]
- [89]. Topgaard D, Diffusion tensor distribution imaging, *NMR Biomed* 32 (2019), 10.1002/nbm.4066 e4066. [PubMed: 30730586]

- [90]. Yon M, de Almeida Martins JP, Bao Q, Budde MD, Frydman L, Topgaard D, Diffusion tensor distribution imaging of an in vivo mouse brain at ultrahigh magnetic field by spatiotemporal encoding, *Nmr Biomed* 33 (2020), 10.1002/nbm.4355.
- [91]. Shemesh N, Jespersen SN, Alexander DC, Cohen Y, Drobniak I, Dyrby TB, et al. , Conventions and nomenclature for double diffusion encoding NMR and MRI, *Magn Reson Med* 75 (2016) 82–87, 10.1002/mrm.25901. [PubMed: 26418050]
- [92]. Yang QX, Smith MB, Wang J. Magnetic Susceptibility Effects in High Field MRI. In: Robitaille P-M, Berliner L, editors. *Ultra High Field Magn. Reson Imaging*, Boston, MA: Springer US; 2006, p. 249–84. 10.1007/978-0-387-49648-1_9.
- [93]. Trattng S, Springer E, Bogner W, Hangel G, Strasser B, Dymerska B, et al. , Key clinical benefits of neuroimaging at 7T, *NeuroImage* 168 (2018) 477–489, 10.1016/j.neuroimage.2016.11.031. [PubMed: 27851995]
- [94]. Trattng S, Bogner W, Gruber S, Szomolanyi P, Juras V, Robinson S, et al. , Clinical applications at ultrahigh field (7 T). Where does it make the difference?, *NMR Biomed* 29 (2016) 1316–1334, <https://doi.org/10.1002/nbm.3272>. [PubMed: 25762432]
- [95]. Isaacs BR, Mulder MJ, Groot JM, van Berendonk N, Lute N, Bazin P-L, et al. , 3 versus 7 Tesla magnetic resonance imaging for parcellations of subcortical brain structures in clinical settings, *PLoS ONE* 15 (2020), 10.1371/journal.pone.0236208 e0236208. [PubMed: 33232325]
- [96]. Setsompop K, Kimmlingen R, Eberlein E, Witzel T, Cohen-Adad J, McNab JA, et al. , Pushing the limits of in vivo diffusion MRI for the Human Connectome Project, *NeuroImage* 80 (2013) 220–233, 10.1016/j.neuroimage.2013.05.078. [PubMed: 23707579]
- [97]. Jones DK, Alexander DC, Bowtell R, Cercignani M, Dell'Acqua F, McHugh DJ, et al. , Microstructural imaging of the human brain with a “super-scanner”: 10 key advantages of ultra-strong gradients for diffusion MRI, *NeuroImage* 182 (2018) 8–38, 10.1016/j.neuroimage.2018.05.047. [PubMed: 29793061]
- [98]. Hennel F, Michael ES, Pruessmann KP, Improved gradient waveforms for oscillating gradient spin-echo (OGSE) diffusion tensor imaging, *NMR Biomed.* 34 (2021), 10.1002/nbm.4434 e4434. [PubMed: 33124071]
- [99]. Solomon E, Liberman G, Nissan N, Frydman L, Robust diffusion tensor imaging by spatiotemporal encoding: Principles and in vivo demonstrations, *Magn. Reson. Med* 77 (2017) 1124–1133, 10.1002/mrm.26197. [PubMed: 26968710]
- [100]. Wu D, Liu D, Hsu YC, Li H, Sun Y, Qin Q, et al. , Diffusion-prepared 3D gradient spin-echo sequence for improved oscillating gradient diffusion MRI, *Magn. Reson. Med* 85 (2021) 78–88, 10.1002/mrm.28401. [PubMed: 32643240]
- [101]. Yon M, Bao Q, Chitrit OJ, Henriques RN, Shemesh N, Frydman L, High-Resolution 3D in vivo Brain Diffusion Tensor Imaging at Ultrahigh Fields. Following Maturation on Juvenile and Adult Mice, *Front. Neurosci* 14 (2020), 10.3389/fnins.2020.590900.
- [102]. Tax CMW, Bastiani M, Veraart J, Garyfallidis E, Okan IM, What’s new and what’s next in diffusion MRI preprocessing, *NeuroImage* 249 (2022), 10.1016/j.neuroimage.2021.1188301 18830.

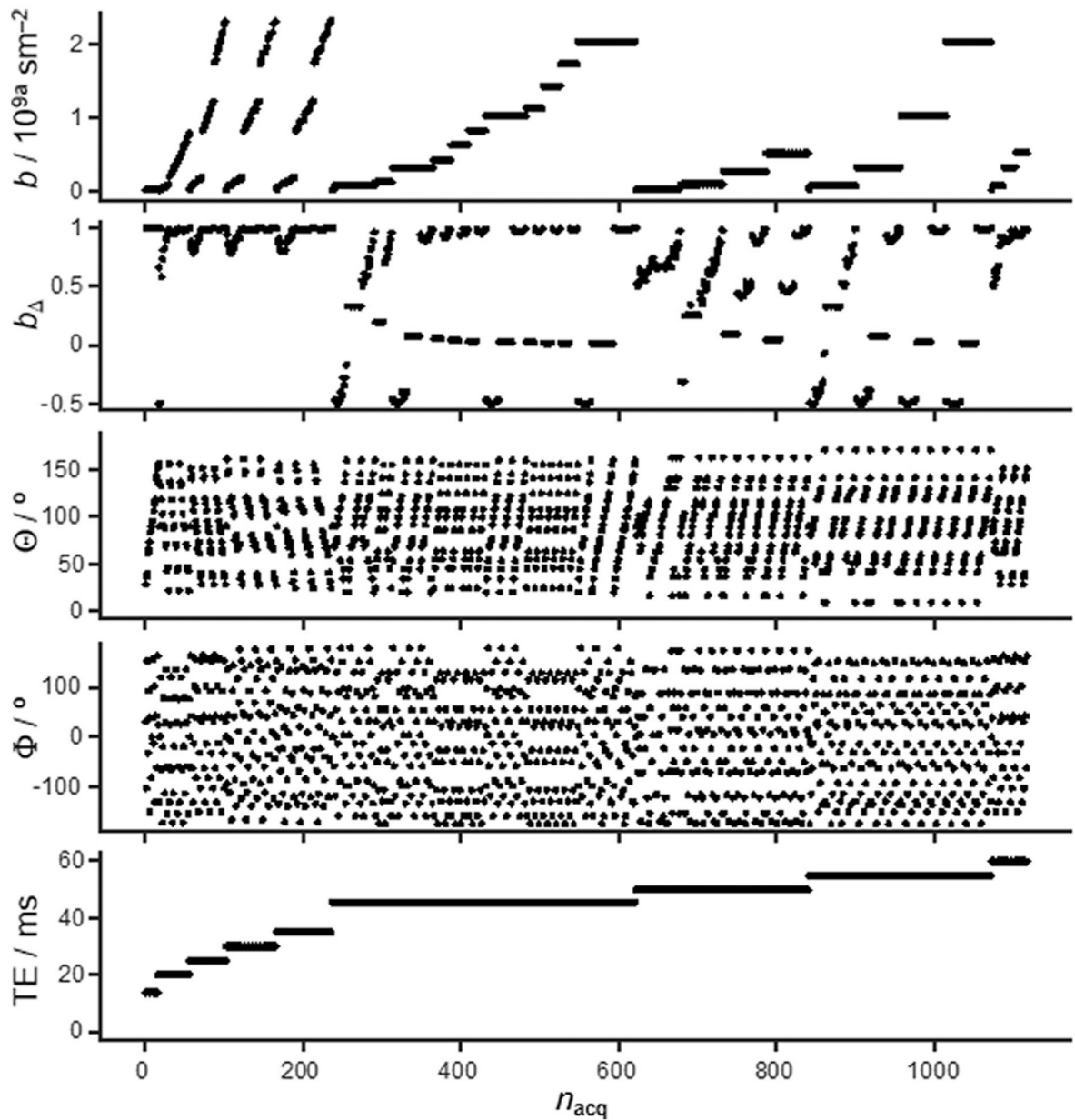


Fig. 1. Acquisition scheme for 5D \mathbf{D} - R_2 distribution MRI. Images are recorded as a function of the magnitude b , normalized anisotropy b (defined in Eq. (3)) and orientation (Θ, Φ) of the b -tensor, as well as the echo time τ_E at constant repetition time τ_R of 5 s. All panels share the same abscissa, where n_{acq} is the acquisition number sorted in the order of ascending τ_E , b , and b .

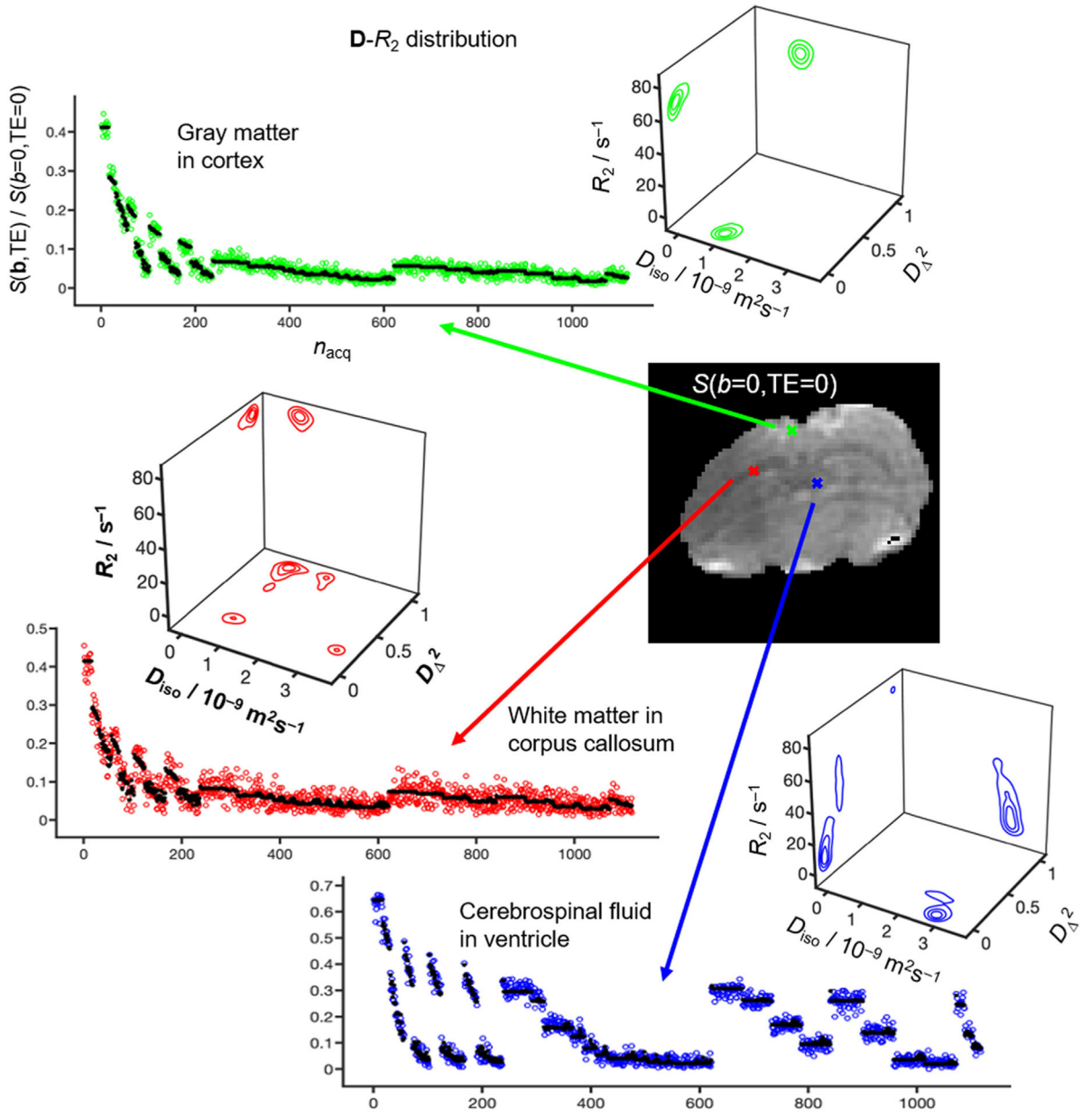


Fig. 2. Experimental results for representative WM (red), GM (green) and CSF (blue) voxels of an *in vivo* rat brain at 21.1 T. The signal S is shown as a function of the acquisition number n_{acq} according to the scheme in Fig. 1 (color-coded circles: experimental, black dots: fit). Nonparametric 5D \mathbf{D} - R_2 distributions obtained by Monte Carlo data inversion of Eq. (4) are visualized as projections onto the 2D $D_{iso} - D_{\Delta}^2$, $D_{iso} - R_2$, and $D_{\Delta}^2 - R_2$ planes, where D_{iso} is the isotropic diffusivity, D_{Δ}^2 the squared normalized anisotropy defined in Eqs. (6)–(7), and R_2 is the transverse relaxation rate.

Author Manuscript

Author Manuscript

Author Manuscript

Author Manuscript

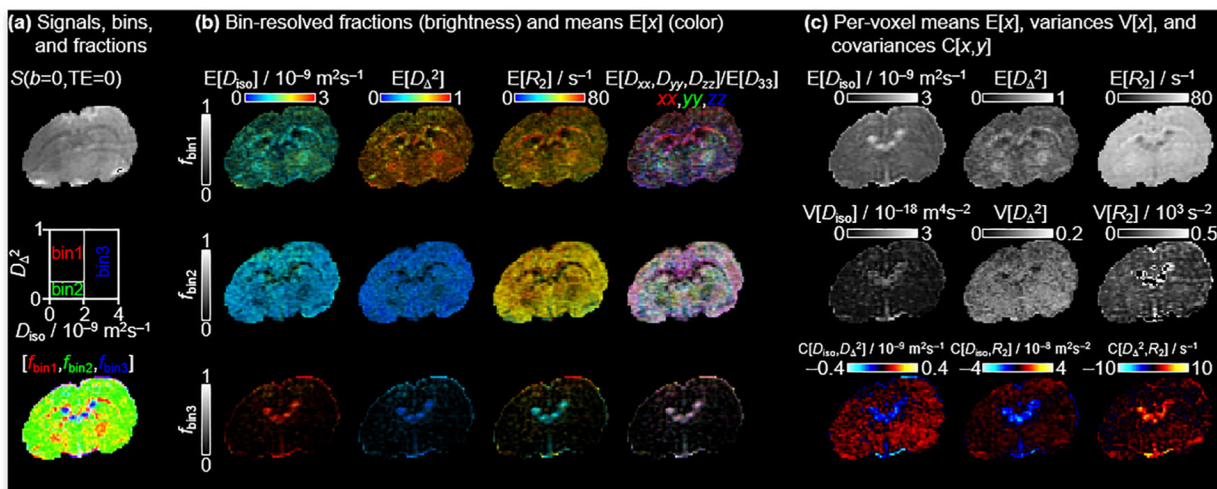


Fig. 3.

Quantitative parameter maps derived from the per-voxel 5D D - R_2 distributions. (a) S_0 image obtained by Eq. (5). Image segmentation is performed by dividing the 2D $D_{iso} - D_A^2$ plane into three “bins” and calculating signal fractions $[f_{bin1}, f_{bin2}, f_{bin3}]$ mainly reporting on the spatial distributions of WM, GM and CSF. Here, blue refers to CSF, red to WM and green to GM. (b) Bin-resolved signal fractions and means $E[x]$ over the D_{iso} , D_A^2 , and R_2 dimensions according to Eq. (8). The bin fractions and means are coded into brightness intensity, and the properties of interest are represented by the color scales, which are each combined by two orthogonal scales in the image. Direction-encoded colors derive from the lab-frame diagonal values $[D_{xx}, D_{yy}, D_{zz}]$ and maximum eigenvalue D_{33} . (c) Per-voxel means $E[x]$, variances $V[x]$ and covariances $C[x,y]$ of various combinations of D_{iso} , D_A^2 , and R_2 are as defined in Eqs. (8–10).

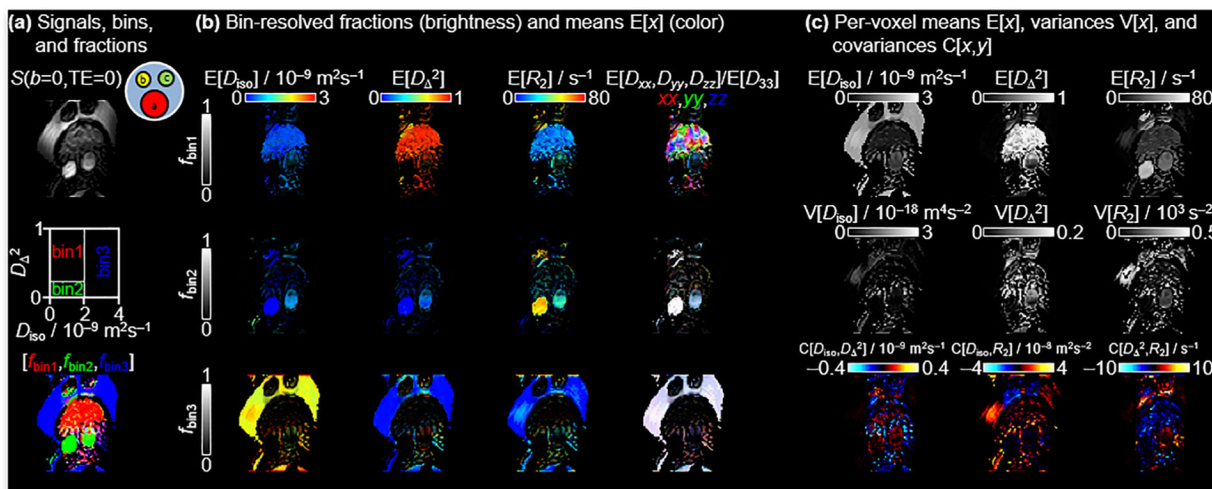


Fig. 4. Parameter maps for the composite phantom comprising an assembly of tubes with liquid crystal (red tube in **4a** phantom cartoon), hydrocarbons (1-octanol and n-dodecane, shown as yellow and green tubes respectively in **4a** phantom cartoon) and water having diffusion properties similar WM, GM and CSF, respectively. See caption of Fig. 3 for detailed explanation of the panels and legends. Image distortions are exacerbated by susceptibility artifacts and chemical shift displacement of the two hydrocarbons not seen *in vivo*.